

Numerical Investigation of Side-Effects due to Fuel Outflow from Secondary Nozzles in Bleed Engine and Gas Generator Cycles of a Retro Propulsion-Assisted Launch Vehicle

Yannik Feldner^{*†}, Moritz Ertl^{*}, Sebastian Karl^{*} and Tobias Ecker^{*}

^{*}German Aerospace Center (DLR), Institute of Aerodynamics and Flow Technology, Spacecraft Department
Bunsenstr. 10, 37073 Goettingen, Germany

yannik.feldner@dlr.de · moritz.ertl@dlr.de · sebastian.karl@dlr.de · tobias.ecker@dlr.de

[†]Corresponding author

Abstract

The effects of cold fuel outflow from secondary nozzles in bleed engine and gas generator cycles on the heat flux distribution along the the baseplate of a reusable launch vehicle are generally ignored in research on launch vehicles. In this work we address this question with numerical simulations of the flowfield. We compare configurations with and without secondary nozzle outflows and show that the predicted thermal loads in the observed region of the vehicle are significantly reduced due to an entrainment of the secondary nozzle flow. We furthermore investigate the differences between a bleed nozzle configuration and a gas generator configuration and we analyse the behaviour over different points of the ascent trajectory of the vehicle. Our work demonstrates the importance of including secondary nozzles in heat flux predictions for launchers.

Keywords: Reusable launch vehicle, retro-propulsion, bleed nozzle, thermal loads, aerothermal, RANS, supersonic exhaust jet, gas generator, baseplate, post-combustion, chemical modelling, Spalart-Allmaras

1. Introduction

Reusable launch vehicles (RLV) have the potential to be a resource- and cost-efficient alternative to conventional space transport systems. While several actors in the sector of space transportation are in the maturing process or already established RLVs as the first stages of their launchers, including Rocket Lab with Neutron² and SpaceX with Falcon 9,⁴ the European long term strategy aims towards the development and characterization of RLV relevant technologies for their next generation of launchers. Among these projects with the goal of investigating Vertical Take-off Vertical Landing (VTVL) launch vehicles is the EU funded Retro Propulsion Assisted Landing Technologies (RETALT)⁹ cooperation. In context of this project two distinct configurations for a Two Stage To Orbit (TSTO) and a Single Stage To Orbit (SSTO) vehicle were investigated. We are basing our studies on a simplified version of the TSTO RETALT1 vehicle. The mission plan for the RETALT1-vehicle is to inject a payload of 20 t into a low earth orbit and to return the first stage to the launch pad or a drone ship via a re-entry burn and a retro propulsion maneuver. During the ascent and retro propulsion phase, high thermal loads are acting on the rocket structure and especially on the landing legs, the baseplate and the aerodynamic control surfaces. These thermal loads are caused by the main engine exhaust of the RLV and have been characterized in a previous study by Laureti et al.⁸

As far as the authors are aware, no published research has been devoted to the topic of side-effects due to the outflow of gas generators, bleed nozzles and air vents of cryogenic fuel tanks in VTVL or other launcher configurations. Owing to these secondary exhaust jets, unburned hydrogen is ejected near the high temperature outflow of the main engines, which could lead to a change in flow characteristics and base heating in the aft-bay region of the vehicle. In order to fill this knowledge gap and provide an assessment of the additional influence due to the secondary nozzle exhaust, steady-state CFD simulations are carried out for different points along the ascent trajectory and varying outflow conditions of the bleed nozzles.

The main focus of this publication is the characterization of the thermal loads and the heat flux distribution along the vehicle baseplate. The flow field solutions and observed phenomena for a configuration with active and deactivated secondary nozzles are compared. In this context, the influence of varying engine cycles and exhaust gas mixtures is studied.

SIDE-EFFECTS OF SECONDARY NOZZLES IN BLEED ENGINE AND GAS GENERATOR CYCLES OF RLVS

In addition, the validity of the computational mesh is confirmed by conducting a grid convergence study and providing an estimate on the numerical uncertainties.

2. Numerical Methods

The influence of exhaust gas from secondary nozzles on thermal loads of Reusable Launch Vehicles (RLV) is observed by using CFD simulations for a set of representative flow conditions along the flight trajectory. These conditions are based on the aero-thermal database of the RETALT1 vehicle derived by Laureti et al.⁸ Since the exhaust gas of the secondary nozzles is used to drive the turbines of the oxidizer and fuel pumps, only flow conditions during the propelled flight phases are relevant. All numerical simulations in this work are done by using the DLR TAU code.¹⁰

2.1 DLR-TAU-Solver and Numerical Settings

The DLR TAU code is a second-order finite-volume flow solver for 2D and 3D problems on hybrid structured-unstructured meshes. TAU uses an edge-based dual-cell approach based on a vertex-centered scheme.

In order to generate comparable results to the already existing aero-thermal database, the Reynolds Averaged Navier Stokes (RANS) equations together with the one-equation Spalart-Allmaras linear eddy viscosity turbulence model¹² are used for steady simulations of the flowfield. This turbulence model yields satisfactory results for the exhaust plume structure of RLVS during their flight trajectory⁵ and is suitable for the prediction of wall heat fluxes in hypersonic flow regimes,⁷ while still being numerically robust.

Second-order spatial accuracy is achieved by applying the AUSMDV¹⁵ upwind flux splitting scheme and a least squares gradient reconstruction, while the temporal discretization is done with a 3-stage explicit Runge-Kutta method.

To improve the numerical accuracy for low Mach number regions, the low-Mach number variable reconstruction modification by Thornber¹⁴ is applied.

Due to the fuel rich outflow of the main engines and secondary bleed nozzles, the potential effects of post-combustion are considered and the chemistry modelling is done by using a reduced Jachimowski mechanism.⁶

2.2 Numerical Setup and Boundary Conditions

2.2.1 Mesh and Boundary Conditions

The simulations are done using a reduced half model of the RETALT1-vehicle without the aerodynamic control surfaces and landing legs on a 3D computational mesh Fig. 1 with 49M volume elements. The reduced vehicle, which will just be referred to as RETALT1 in the following, is enclosed by a spherical farfield mesh with radius $r_{ff} \approx 280$ m to capture the full plume structure and shock formation for supersonic flight Mach numbers. Cylindrical and conical grid refinement regions are used at the aft bay of the rocket to provide a high spatial resolution of the exhaust jets. Since the main focus of this work is to characterize the thermal loads on the rocket baseplate and the resulting flow structures, only the first stage is simulated. Therefore, a generic payload fairing was added on top of the vehicle to create a realistic configuration and prevent flow disturbances for the ascent trajectory. The simulated trajectory points, together with the flight Mach number are given in tab.(1).

Table 1: Simulated trajectory points and flight Mach number.

Trajectory point	height [km]	Mach number	ambient pressure [Pa]
Ascent 1	7	0.8	41060.7
Ascent 2	35	2.8	475.9
Ascent 3	60	4.5	20.3
Ascent 4	86	7.4	0.3

The computational domain is initialized using a dry air single species mixture with the mass fractions of $N_2 = 76.7\%$ and $O_2 = 23.3\%$. As in the aerothermal database,⁸ all simulations are done for a wall temperature of 600 K.

The exit diameter of the RETALT1 main engine and bleed nozzle are given by $D_{main} = 1.1$ m and $D_{BN} = 0.14$ m while the outflow is defined through a supersonic outflow boundary condition. The bleed nozzles are arranged in a ring shape between the central nozzle and the 8 outer main engines, in such a way, that the angle between the vector connecting the bleed nozzle and the nearest main engine in positive y-direction and the vector connecting the engine

SIDE-EFFECTS OF SECONDARY NOZZLES IN BLEED ENGINE AND GAS GENERATOR CYCLES OF RLVs

with the central engine equals 45° (see Fig. 1 d)). This arrangement allows to reduce the full model to a half model with only 4 annular and one central bleed nozzle. These outer bleed nozzles stand out from the baseplate by a height of $h_{\text{BN}} = 0.03 \text{ m}$. The central main engine and the bleed nozzle connected to it are elevated by $\Delta h_{\text{main}} = 0.15 \text{ m}$ and $\Delta h_{\text{BN}} = 0.4 \text{ m}$, respectively.

2.2.2 Derivation of the Bleed Nozzle Exit Conditions

In order to investigate the influence of additional gas outflow from secondary nozzles in RLV-configurations, which is used to power the oxidizer and fuel pumps, two main engine cycles were identified as suitable modelling options. An expander bleed engine and a gas generator cycle, as they represent two state-of-the-art liquid propellant engine cycles. In both cases only little or no consistent information on detailed engine configurations combined with secondary nozzle outflows are available. The outflow conditions were derived by comparing and rescaling engine cycles with similar thrust and exit conditions, respectively. In this section, the rescaled conditions for the expander bleed engine cycle are derived by using the reference values from the work of Sippel et al.¹¹ presented in tab.(2) and a short description of the cycle is given.

Table 2: Reference values for the main engine and bleed nozzle outflow taken from Sippel et al.¹¹

Properties	Units	Main engine	bleed nozzle 1	bleed nozzle 2
Mass flow	kg/s	539.29	2.649	8.06
Temperature	K	1579	230.15	214.83
Mach number	–	3.411	1.973	1.975
Exit velocity	m/s	3799.77	2240.18	2160.55
Exit pressure	bar	0.6	0.4	0.4

In a bleed engine cycle, cryogenic hydrogen from the fuel tank is pumped through the cooling channels of the main engines thrust chamber and nozzle walls, heats up and expands. The heated hydrogen gas is used to drive the two separate turbines for the oxidizer and fuel pumps and is then ejected through secondary bleed nozzles. The exit conditions for the bleed nozzles in the reference case are characterized by the mass flow, the temperature and the exit pressure.

For the simulations of the RETALT1 bleed nozzles, similar temperatures and exit velocities compared to the reference case are desired. Therefore, the exit temperature and velocity are set to $T_e = 230.15 \text{ K}$ and $v_e = 2240.18 \text{ m/s}$. The rescaling of the exit conditions is done by calculating the ratio of the mass flow rates for the corresponding main engines. In case of RETALT1 the main engine mass flow equals $\dot{m}_{\text{main}} = 315.81 \text{ kg/s}$, while the mass flow for the reference case is given by $\dot{m}_{\text{ref}} = 539.29 \text{ kg/s}$, which leads to a mass flow ratio of:

$$r_{\dot{m}} = \frac{\dot{m}_{\text{main}}}{\dot{m}_{\text{ref}}} \approx 0.59 \quad (1)$$

Since the RETALT1 configuration only uses a single bleed nozzle per main engine, the mass flow for the reference case is combined and rescaled to create a single outflow condition:

$$\dot{m}_{\text{BN,RET}} = r_{\dot{m}} \dot{m}_{\text{ref}} = 6.27 \frac{\text{kg}}{\text{s}} \quad (2)$$

The exit Mach number of the bleed nozzle is calculated via:

$$M_e = \frac{v_e}{\sqrt{\gamma R T_e}} = 1.94 \quad (3)$$

with $R = 4124 \text{ J/(kg K)}$ and $\gamma = 1.41$ being the specific gas constant and heat capacity ratio for hydrogen, respectively. The Mach number, together with the exit pressure $P_e = 0.4 \text{ bar}$ in the reference case, are used to calculate the total pressure in the combustion chamber, resulting in $P_c = 2.84 \text{ bar}$.

The throat area for the previously defined RETALT1 bleed nozzle, with corresponding exit area of $A_e = 0.063 \text{ m}^2$ is given by:¹³

$$A_t = A_e M_e \left[\frac{1 + \frac{\gamma-1}{2} M_e^2}{\frac{\gamma+1}{2}} \right]^{-\frac{\gamma+1}{2(\gamma-1)}} = 0.039 \text{ m}^2. \quad (4)$$

SIDE-EFFECTS OF SECONDARY NOZZLES IN BLEED ENGINE AND GAS GENERATOR CYCLES OF RLVS

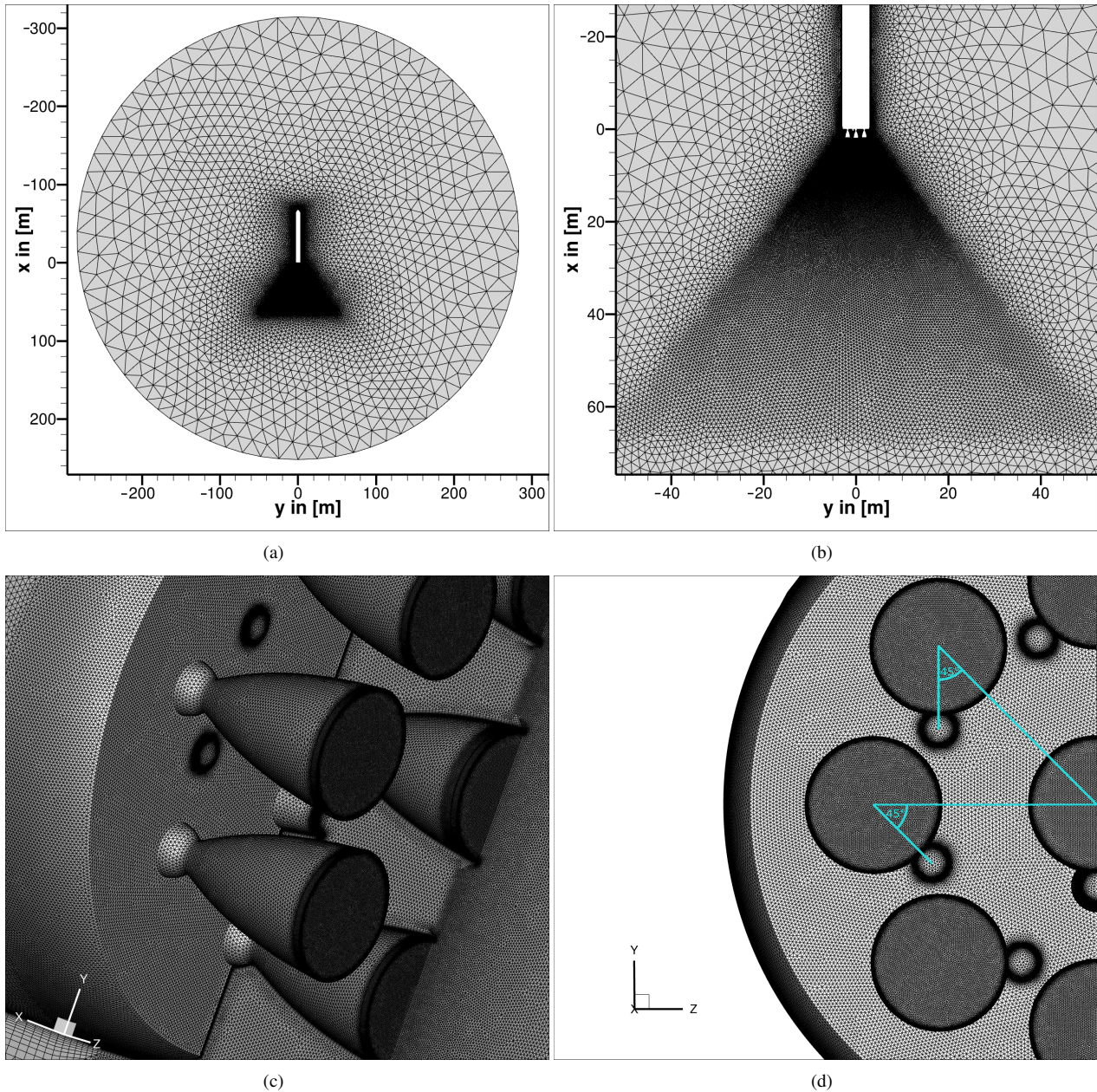


Figure 1: a) View of the symmetry plane of the full mesh. b) Refinement region for the exhaust plumes in the symmetry plane. c) 3D view on the aft-bay region of the vehicle and visualization of the main and bleed nozzles. d) Baseplate of the reduced RETALT1-vehicle with schematic representation of the bleed nozzle arrangement.

SIDE-EFFECTS OF SECONDARY NOZZLES IN BLEED ENGINE AND GAS GENERATOR CYCLES OF RLVS

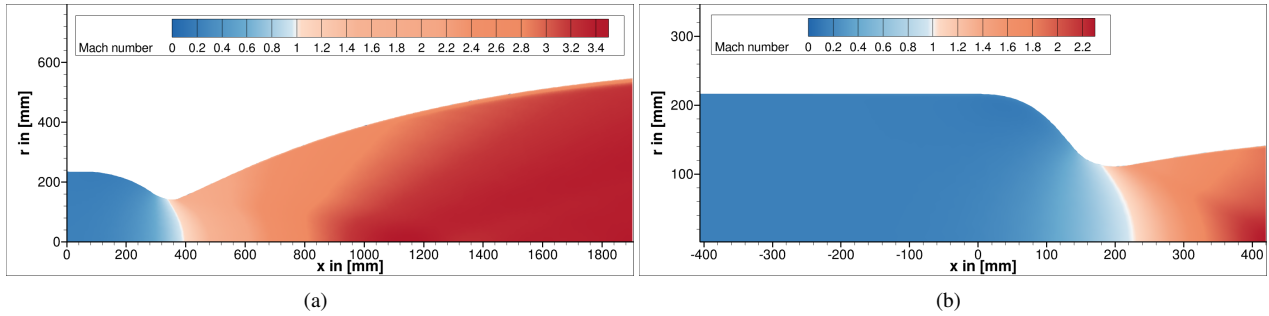


Figure 2: a) Main engine Mach number distribution. b) Bleed nozzle Mach number distribution.

The density inside the combustion chamber is calculated with the ideal gas law together with a total temperature of $T_t = 312.7$ K, leading to a value of $\rho_c \approx 0.17$ kg/m³.

2.2.3 Derivation of the Gas Generator Exit Conditions

The second approach for modelling the outflow conditions of the side nozzles is to utilize a gas generator cycle. Since the chamber conditions for the RETALT1 main engines are similar to the Vulcain engine, the technical characteristics for the corresponding gas generator can be taken from the work of Brossel et al.¹

A fuel rich mixture of liquid hydrogen, liquid oxygen with an oxidizer to fuel ratio of $\frac{O}{F} = 0.9$ is burned in the gas generator, so that the outlet temperature is below the melting point of the turbine blades. The hot exhaust gas is then used to power the oxidizer and fuel pumps. For the sake of simplicity, only the hydrogen turbopump will be considered for an estimation of the inflow conditions of the bleed nozzle.

The characteristics for the hydrogen turbopump are given by a turbine gas inlet pressure and temperature of $P_{in} = 75$ bar, $T_{in} = 900$ K and the heat capacity of $c_p = 8083.3$ J/(kg K). Together with the change in enthalpy, given through the turbine power of $P = 12$ MW and the mass flow of $\dot{m} = 9.2$ kg/s, the turbine outlet temperature $T_{out} = 723$ K can be calculated from the enthalpy difference. The chamber pressure can be derived by an isentropic expansion leading to a value of $P_{out} = 35.4$ bar, with a heat capacity ratio of $\gamma = 1.37$ for the exhaust mixture, while the density can be calculated with the ideal gas law giving a value of $\rho_{out} = 2.26$ kg/m³.

These nozzle inlet conditions lead to a significantly increased mass flow for the secondary nozzles in separate simulations (see sec.(2.2.4)). Therefore, the chamber inflow density is adjusted with respect to the diameter and the mass flow leading to a value of $\rho_{out} = 0.4$ kg/m³. The adjusted inlet pressure equals $P_{out} = 3.32$ bar.

2.2.4 Nozzle Simulation

The outflow conditions and profiles of the RETALT1 main and the secondary nozzles were generated by conducting separate, 2D-axisymmetric nozzle simulations. For the main engine, the combustion chamber inflow consists of a mixture of liquid hydrogen and oxygen with an oxidizer to fuel ratio of $\frac{O}{F} = 6.7$. The reduced Jachimowski mechanism is applied to all simulations. The chamber conditions are characterized by the pressure $P_c = 117.3$ bar and the total density of $\rho_c = 5.44$ $\frac{\text{kg}}{\text{m}^3}$.

Since the exhaust gas of the secondary nozzles in the bleed engine cycle only consists of hydrogen, the corresponding simulations were done for a single species transport with the chamber conditions derived in sec.2.2.2 ($P_c = 2.84$ bar, $\rho_c = 0.17$ $\frac{\text{kg}}{\text{m}^3}$). A generic nozzle contour for the bleed engine is created by using the derived supersonic area ratio of $r_{sup} = \frac{A_e}{A_t} = 1.62$. The same nozzle contour was used for the simulations with the boundary conditions of the gas generator cycle. The results are given in Fig. 2.

Linear interpolation is used to map the generated nozzle outflow profiles as dirichlet condition onto the corresponding boundary markers of the 3D simulations of the RETALT1 vehicle.

2.3 Grid Convergence Study

The quality of the numerical mesh is verified by conducting a grid convergence study utilizing the Grid Convergence Index or GCI-methodology proposed by Celik et al.³ in the ASME-standard. For this, three different grids with varying cell size in the refinement region of the exhaust plume are generated. The fine, medium and coarse grid consist

SIDE-EFFECTS OF SECONDARY NOZZLES IN BLEED ENGINE AND GAS GENERATOR CYCLES OF RLVS

of $N_1 = 108$ M, $N_2 = 49$ M and $N_3 = 27$ M volume elements, respectively. The first layer thickness of the numerical meshes is kept constant in order to guarantee a dimensionless wall distance of $y^+ < 1.0$, which is required for simulations with one-equation Spalart-Allmaras turbulence models without wall functions. The calculation of the refinement factors is done by comparing the representative, mean cell size between the three meshes leading to a value of $r_{21} = 1.36$ for the medium and fine mesh and $r_{32} = 1.33$ for the medium and coarse mesh, which is in range of the suggested value of $r > 1.3$.

The coarse- and fine-grid GCI, together with the relative errors e_a and extrapolated relative errors e_{ext} are calculated for the Mach number and temperature variables of the flow field and the wall heat flux along the RETALT1-baseplate in tab.(3). The small relative errors and GCI-values of the field variables, in addition to the high amount of oscillatory convergence concerning the temperature field, indicate that the results on the different meshes are in good agreement. This can be verified by comparing the flow field and profile lines of the Mach number and temperature in Fig. 3, showing that the overall characteristics remain the same, while the shock distances and intensities are slightly underestimated for coarser meshes due to the high resolution needed in these areas.

Owing to the pointwise comparison for the surface values of the significantly coarser meshes, the relative errors of the heat flux values along the baseplate increase, while the GCI is about 4%. In order to estimate an error independent of the local spacing and preserving high gradients in the heat flux distribution, the relative error of the integrated heat flux is calculated, leading to values of 2.15% for the medium and fine mesh and 1.3% for the medium and coarse mesh. The heat flux distribution along the baseplate of the RETALT1-vehicle is given in Fig. 4.

These results lead to the conclusion, that the solution on the numerical meshes is converged. Therefore, the resolution on the medium grid, which is used for the subsequent simulations, is sufficient to capture the occurring flow characteristics and heat flux distributions in the aft-bay region of the vehicle.

Table 3: GCI Results and relative errors of the integrated heat flux.

mean error in %	Mach-Field	Temp.-Field	Baseplate heat flux
e_a^{21}	1.62	1.24	12.27
e_{ext}^{21}	0.83	0.67	3.52
GCI_{fine}^{21}	1.01	0.84	4.39
e_a^{32}	1.29	0.80	5.06
e_{ext}^{32}	0.95	0.56	3.51
GCI_{coarse}^{32}	1.16	0.70	4.05
rel. error int. heat flux $\frac{\text{fine}}{\text{medium}}$	–	–	2.15
rel. error int. heat flux $\frac{\text{med}}{\text{coarse}}$	–	–	1.30
oscillatory conv.	25.70	83.55	46.85
apparent order p	16.11	14.19	13.25

[†] superscript ²¹: error medium-fine mesh; superscript ³²: error coarse-medium mesh

SIDE-EFFECTS OF SECONDARY NOZZLES IN BLEED ENGINE AND GAS GENERATOR CYCLES OF RLVS

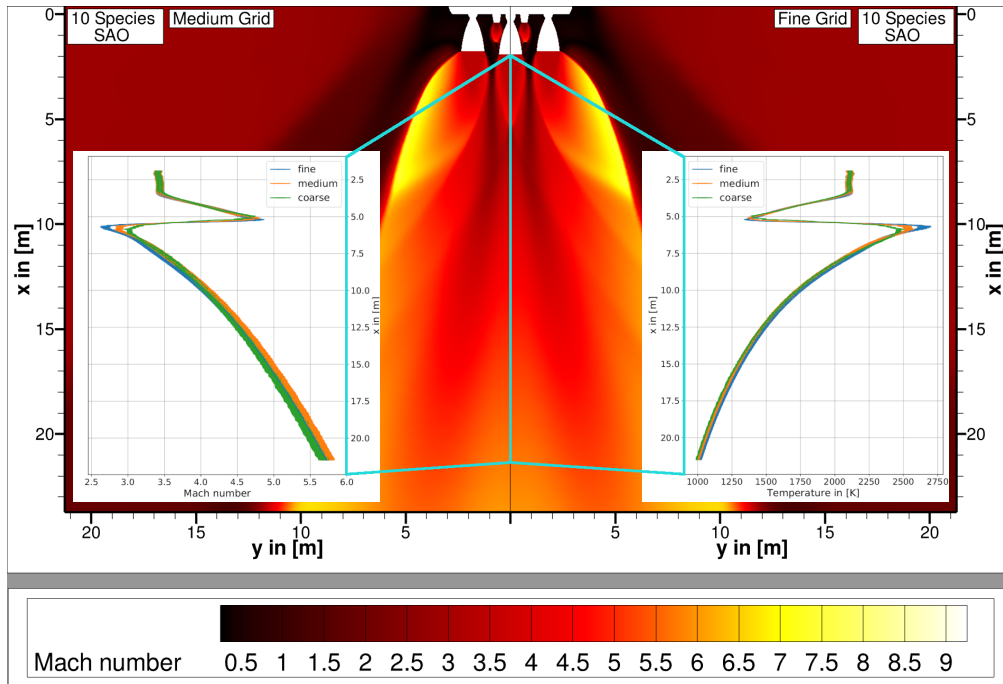


Figure 3: Comparison of the flow fields for the solution on the medium and fine mesh, including the temperature and Mach number profile along the center line. The simulations were done using a 10 species mixture and the Spalart-Allmaras (SAO) turbulence model.

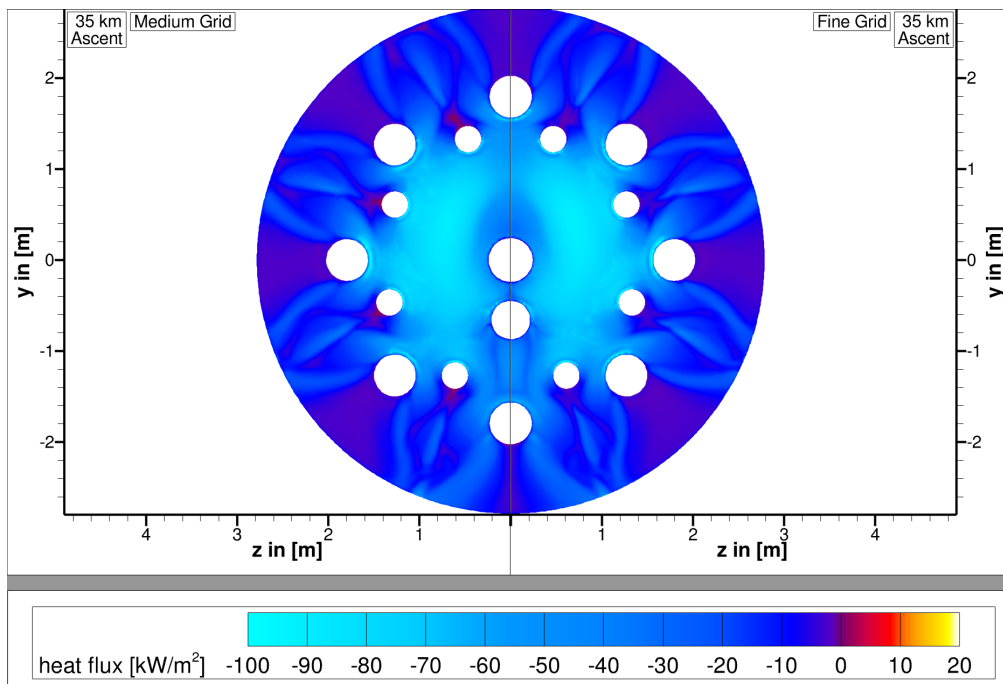


Figure 4: Comparison of the heat flux distribution along the baseplate of the RETALT1-vehicle for the solution on the medium and fine mesh.

3. Results

The CFD results for analysing the baseplate heat flux of the reduced RETALT1 vehicle cover the ascent trajectory from an altitude of 7 km up to 86 km for the trajectory points given in tab.(1). During this phase, the thermal loads in the aft-bay region are dominated by the exhaust gas from the main engines and bleed nozzles. For the ascent phase all

SIDE-EFFECTS OF SECONDARY NOZZLES IN BLEED ENGINE AND GAS GENERATOR CYCLES OF RLVS

engines of the first stage are active, leading to an outflow of exhaust gas from $N_1 = 3 + \frac{3}{2}$ of the main engines in the half model and the $N_2 = 4 + \frac{1}{2}$ bleed nozzles.

A reference case for an altitude of 35 km is defined. The reference case is used to characterize the overall influence of active secondary nozzles in contrast to simulations without additional fuel outflow and to compare the results for the bleed engine cycle with the gas generator cycle in the following two sections. Afterwards, the thermal loads for the ascent trajectory will be analyzed.

3.1 The Influence of the additional Bleed Nozzle Outflow

In this section the influence of the bleed nozzle outflow will be analyzed by comparing the results with a configuration in which the bleed nozzles are deactivated. The simulations were done for the reference case at an altitude of 35 km. The flowfields for the two configurations are shown in Fig. 5, while the corresponding heat flux distributions along the baseplate are given in Fig. 6.

In Fig. 5, the Mach number in the symmetry plane together with an iso-surface of negative axial velocities of $u < -200$ m/s is plotted for the configuration without bleed nozzle outflow on the left side and with active bleed nozzles on the right side. In order to give an estimation of the thermal loads caused by the recirculating exhaust gas on the baseplate, the temperature color map is projected onto the iso-surface. The flowfield at an altitude of 35 km is characterized by highly underexpanded jets leading to a large spatial extension and strong plume-plume interactions. In general, the shock characteristics and flowfield structure downstream of the main engine exhaust remain similar in both cases, since the overall mass flow of the bleed nozzles makes up only about 2% of the main engine exhaust.

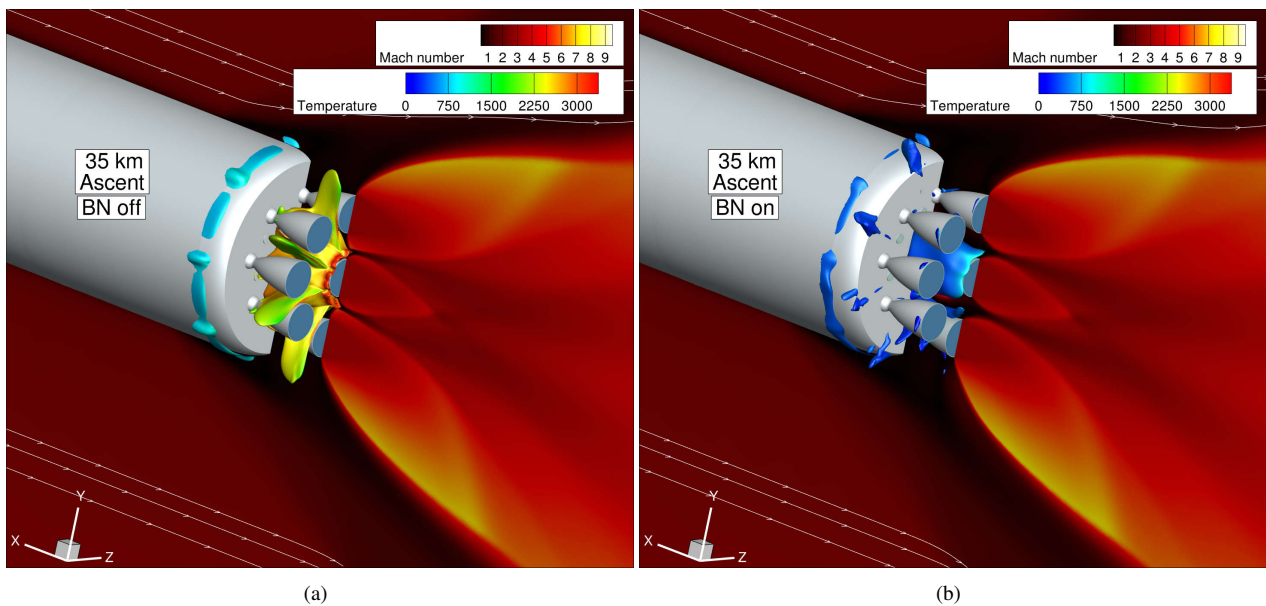


Figure 5: Flowfield represented by the Mach number and iso-surface with negative axial velocity of $u < -200$ m/s for a) the configuration with deactivated bleed nozzles and b) the configuration with active bleed nozzles.

In contrast to this, the additional outflow from the bleed nozzles has a strong effect on the flow structure in the aft bay region and the cavities between the main engines. For deactivated bleed nozzles, a strong recirculation region forms around the central main engine and the gaps between the annular main engines, which leads to the entrainment of hot exhaust gas towards the baseplate of the vehicle. This observation can be supported by the corresponding heat flux distribution in Fig. 6 on the left. For a given wall temperature of 600 K, high thermal loads with local maxima in the range of 180 – 260 kW/m² can be identified between the central nozzle and the outer ring of nozzles in addition to the gaps between them. The maxima are located in front of the nozzle-baseplate intersections of the main engines in positive radial direction. The nozzles themselves have a shielding effect on the baseplate region behind them, where the heat flux is moderately low, up to 20 kW/m². This simulation setup of the reduced RETALT1-vehicle leads to comparable results with the RETALT1 database derived by Laureti et al.⁸ and the same flow field characteristics are observed.

For active bleed nozzles, a significant change in the flowfield and the base heating can be identified. Due to the additional outflow of cold hydrogen with a temperature of $T_e = 230.15$ K and a velocity of $v_e = 2240.18$ m/s, the

SIDE-EFFECTS OF SECONDARY NOZZLES IN BLEED ENGINE AND GAS GENERATOR CYCLES OF RLVS

recirculation and entrainment of hot exhaust from the main engines is prevented in most areas, represented by the iso-surface of the negative velocities in Fig. 5. The bleed nozzle exhaust jets lead to a constriction of the main engine exhaust, which can be seen in the Mach number distribution. The main recirculation region can be identified around the central nozzle further outward of the central or annular bleed nozzles. In contrast to the configuration without bleed nozzle outflow, the temperature of the recirculating gas is significantly reduced and the highest values can be found around the central main engine outlet again. By comparing these results with the heat flux distribution in Fig. 6 on the right side, the cold hydrogen leads to a significant reduction of the heat flux values in range of $[-100;20]\text{kW/m}^2$. The minima are found in the central region close to the bleed nozzles and along the edges of the outer main engines. The cold gas outflow only has a small influence on the heatflux values behind the baseplate openings of the main engines in the peripheral region of the baseplate.

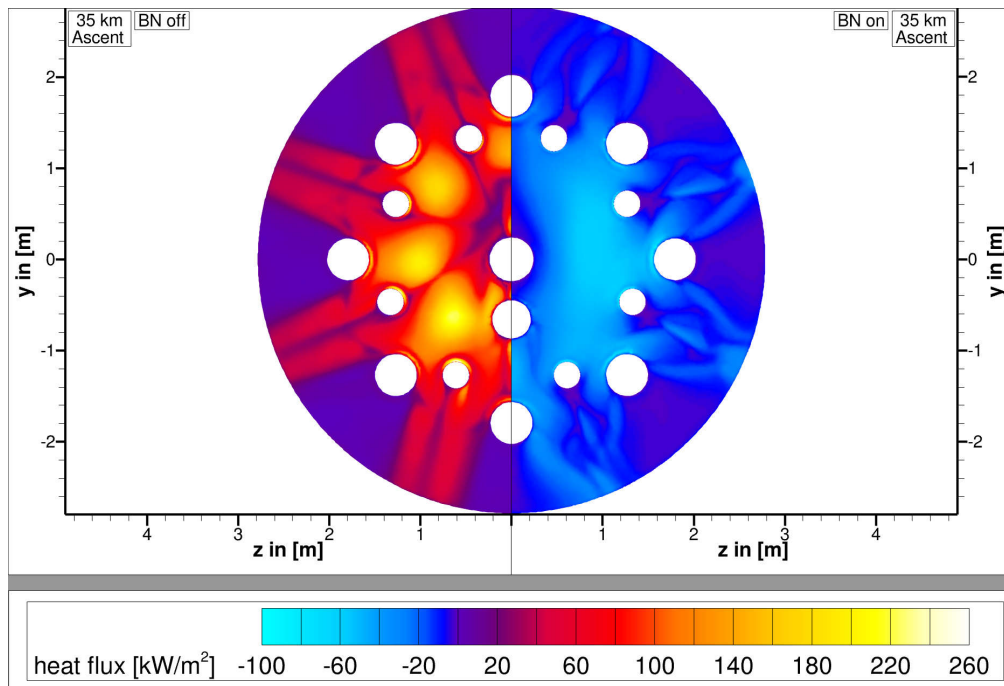


Figure 6: Comparison of the heat flux distribution along the baseplate for an altitude of 35km along the ascent trajectory. Left side: bleed nozzles off, right side: bleed nozzles on.

3.2 Comparison of the Bleed Nozzle and Gas Generator Cycle

Two distinct simulations for the bleed engine and gas generator cycle in the reference case were done using the interpolated nozzle outflow profiles calculated with the chamber conditions derived in sec.(2.2.2) and sec.(2.2.3). The resulting heat flux distributions along the baseplate are shown in Fig. 7.

Although the two engine configurations are characterized by slightly varying mass flows, species mixtures and thermodynamic states, the numerical results only show minor differences in the flowfield structure and heat flux distribution. It was expected, that due to the fuel rich outflow of the secondary nozzles near the hot main engine exhaust, additional combustion with the ambient oxygen would occur. This is not the case and no post-combustion was observed. Therefore, varying the species mixture has no relevant influence on the heat flux distribution. The outlet temperature is approximately the same in both cases and the overall heat flux values remain in the range of $[-100; 20]\text{ kW/m}^2$. Only a small increase in local heat flux can be seen for the gas generator configuration around the central main engine, while the spatial extend of the high heat flux region is reduced, and inside the wake area of the bleed nozzles close to the baseplate edge.

This observation leads to the conclusion that the simpler inflow condition of the bleed engine cycle is sufficient for our study and is therefore used in all subsequent simulations.

SIDE-EFFECTS OF SECONDARY NOZZLES IN BLEED ENGINE AND GAS GENERATOR CYCLES OF RLVS

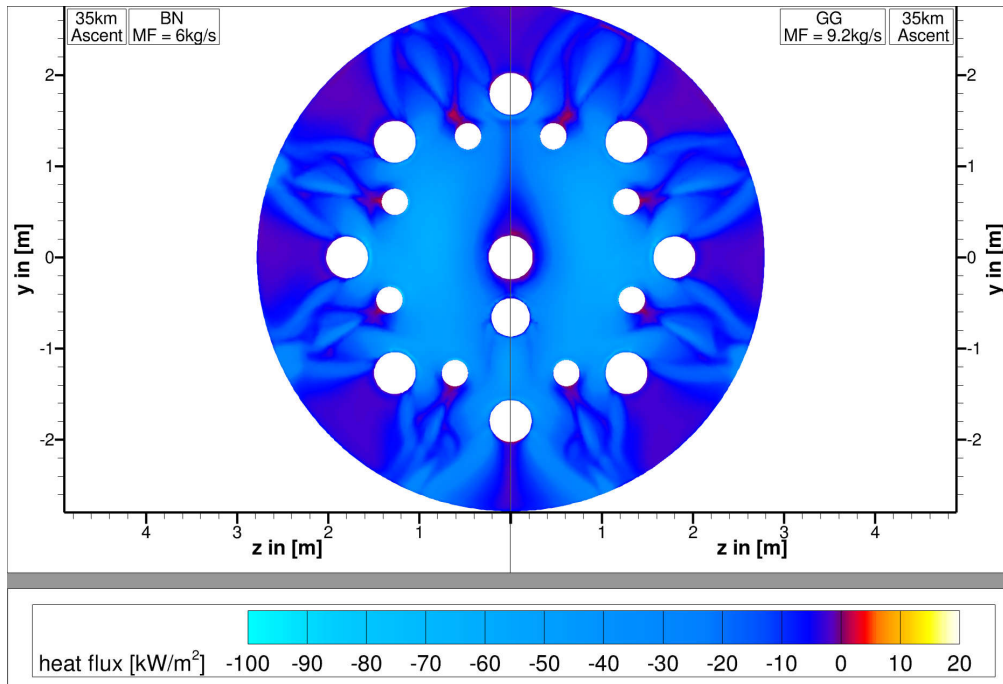


Figure 7: Comparison of the heat flux distribution along the baseplate of the RETALT1-vehicle for the bleed nozzle cycle, with pure hydrogen exhaust and gas generator cycle, with an exhaust mixture of water and hydrogen at slightly higher temperatures.

3.3 Ascent Trajectory

This section discusses the thermal loads on the baseplate for the ascent trajectory. During this phase the varying ambient pressure and flight Mach number lead to a wide range of flow regimes and different characteristics of the exhaust plumes. Representative flowfield visualizations are given in Fig. 8. As in Fig. 5, these plots show the Mach number along the symmetry plane and an iso-surface of negative axial velocity.

For altitudes lower than 7 km the large atmospheric ambient pressure leads to a confined configuration of the supersonic exhaust jets, while the vehicle flight speed is still in the subsonic regime. Only weak plume-plume interactions are observed in close proximity to the main engine outlets, which increases along the downstream direction. In this case, only weak recirculation and backflow towards the baseplate occurs. In order to visualize these regions, the threshold for the negative axial velocity of the iso-surface was set to $u < -25$ m/s, while it was kept at $u < -200$ m/s for the configurations at higher altitudes. The temperature map, which differs from the one used in sec.(3.1), is projected onto the iso-surface.

It can be seen, that the slow, recirculating gas in the peripheral region of the aft bay exhibits temperatures in the range of the bleed nozzle outlet values. It is observed, that due to the impingement of the secondary exhaust jets onto the outer nozzle walls of the main engines flow deflection occurs leading to the entrainment of cold hydrogen. The results for the 7km case were characterized by an unsteady, fluctuating behaviour of the flow along the baseplate, while the overall heat loads remained similar. The heat flux distribution can be seen in Fig. 9 on the left, showing overall negative values in the range of $[-100; -80]$ kW/m² in regions where the bleed nozzle outflow reaches the baseplate. In the area of the central main engine outlet, a slight increase in temperature was observed due to the interaction of the cold hydrogen gas with the exhaust plume.

For increasing altitudes the flow conditions in the aft bay region become more stable. The main engine exhaust, which tends to recirculate in the outlet region of the nozzles, interacts with the additional hydrogen gas from the bleed nozzles and starts to enclose the baseplate region. Due to the higher underexpansion ratio for increasing altitudes, the base area surrounded by the exhaust plumes grows, while the exhaust jet structures in the central region remains the same. This effect leads to similar heat flux distributions in the central baseplate region for the 35km Fig. 9 and 60km Fig. 10 case while the peripheral region shows different characteristics.

Above 60km, the recirculating flow in the base region, which is enclosed by the highly underexpanded main engine exhaust jets, becomes independent of the free stream conditions and the heat flux distribution along the baseplate remains the same. A plot comparing the baseplate heat flux for an altitude of 60km and 86km is given in Fig. 10. Due

SIDE-EFFECTS OF SECONDARY NOZZLES IN BLEED ENGINE AND GAS GENERATOR CYCLES OF RLVS

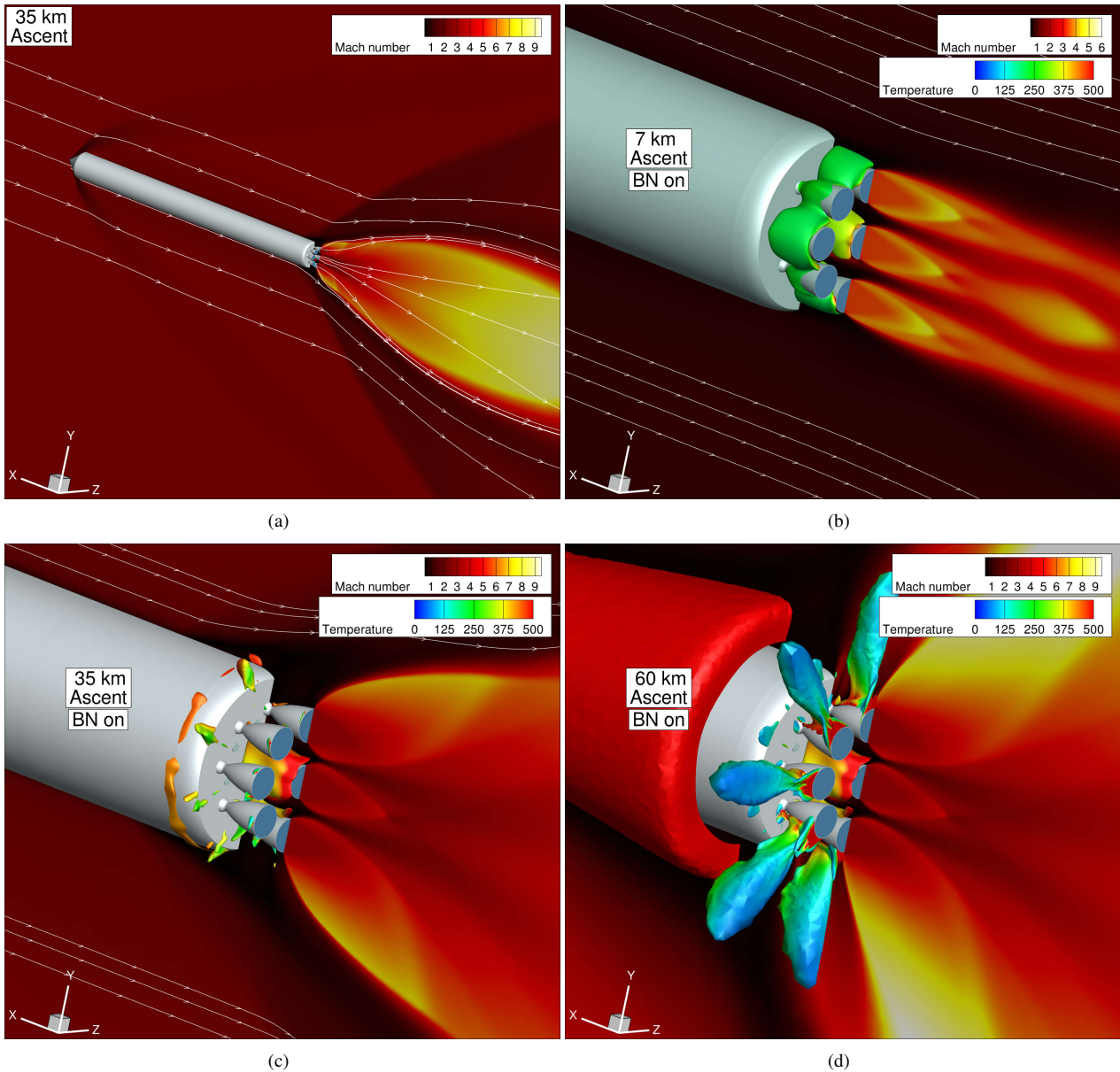


Figure 8: Flowfield visualizations for the ascent trajectory a) full vehicle and plume structure at an altitude of 35 km b) Aft-bay region and iso-surface of negative axial velocity of $u < -25$ m/s for an altitude of 7 km c) Aft-bay region and iso-surface of negative axial velocity of $u < -200$ m/s for an altitude of 35 km d) Aft-bay region and iso-surface of negative axial velocity of $u < -200$ m/s for an altitude of 60 km.

Note: The temperature colorscale for the iso-surface differs from the one in Fig. 5.

SIDE-EFFECTS OF SECONDARY NOZZLES IN BLEED ENGINE AND GAS GENERATOR CYCLES OF RLVS

to the increasing influence of the main engine exhaust, the heat flux in the peripheral aft-bay region increases since there are no bleed nozzles present to prevent the backflow. The heat flux values for higher altitudes are in the range of $[-100;10]$ kW/m².

The results can be divided in two major flow regimes, the low and high altitude configuration. While the low altitude simulations for heights below 7km show confined plumes, weak recirculation and fluctuating heat fluxes on the baseplate, the high altitude configurations in the range of $[35;86]$ km are characterized by stable flow conditions with highly underexpanded exhaust jets and strong plume-plume interaction.

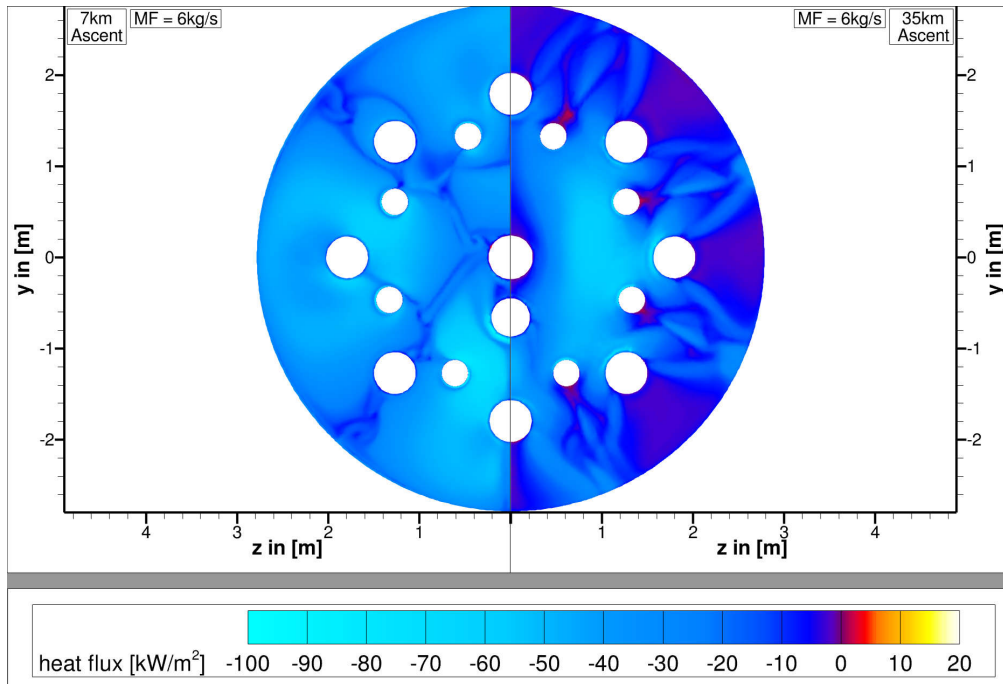


Figure 9: Comparison of the heat flux distribution along the baseplate for altitudes of 7km and 35km.

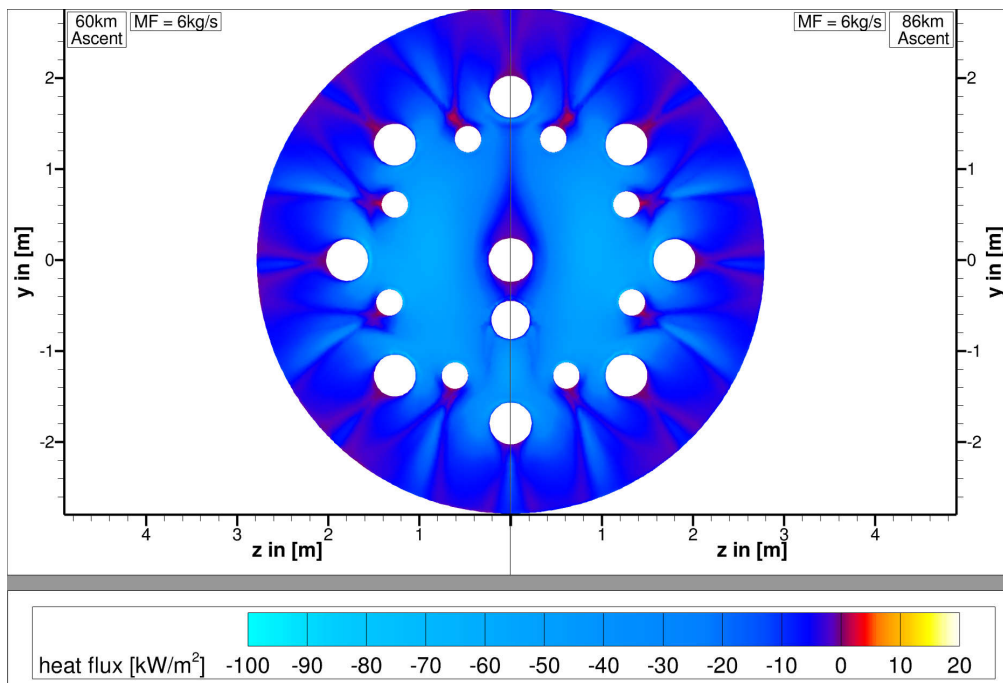


Figure 10: Comparison of the heat flux distribution along the baseplate for altitudes of 60km and 86km

SIDE-EFFECTS OF SECONDARY NOZZLES IN BLEED ENGINE AND GAS GENERATOR CYCLES OF RLVs

The heat flux distribution is dominated by the exhaust plume structure of the main engines and bleed nozzles and becomes independent of the free stream conditions for altitudes above 60km.

4. Conclusions

In this study, the influence of additional fuel outflow from bleed nozzles on the base heating of a reusable launch vehicle were investigated with 3D CFD simulations of the flow field. The simulations were done using steady-state Reynolds averaged Navier Stokes equations together with a one-equation Spalart-Allmaras turbulence model and a reduced Jachimowski mechanism for the chemistry modelling. The numerical methods and setup, as well as the derivation of the boundary conditions for the secondary nozzles were described. A detailed grid convergence study was carried out to verify the numerical quality of the mesh and the numerical errors were estimated.

A reference case for an intermediate altitude of 35 km was chosen to compare the influence of active bleed nozzles to a configuration with deactivated bleed nozzles. Although the additional outflow of cold hydrogen gas from the secondary nozzles in case of active bleed nozzles only makes up about 2% of the main engine exhaust, the high velocities of the underexpanded jets prevent the recirculation of the hot main engine exhaust. This leads to a significant reduction of the thermal loads and heat flux values in the range of $[-100;10]$ kW/m² for a wall temperature of 600 K. In addition two different engine cycles, given by a bleed engine and gas generator cycle, were analyzed for the reference case. The two differing engine cycles only have a small influence on the heat flux distribution along the baseplate leading to overall negative heatflux values. This indicates that the influence of secondary nozzle exhaust, independent of the main engine cycle, is highly relevant for the prediction of heat loads in the aft-bay region of various kinds of launch vehicles and should not be neglected for the aerothermal characterization of these configurations.

Finally, the flowfield and heat flux characteristics for different points along the ascent trajectory of the RLV were investigated, while the descent trajectory will be covered in a subsequent work. During the ascent phase, a wide range of flow regimes can be observed, which are characterized by the flight Mach number and ambient pressure. For lower altitudes, the high ambient pressure results in confined main engine exhaust jets with weak plume-plume interactions in the aft-bay region. Only weak recirculation regions with small velocities can be observed and the heat flux along the baseplate is dominated by the secondary nozzle exhaust. For increasing altitudes strong plume-plume interactions are observed and the highly underexpanded main engine exhaust jets envelope the aft-bay of the vehicle. This leads to a converging characteristic of the heat flux along the baseplate towards the high altitude configuration, where the observed distribution becomes independent of the free stream conditions. This state is reached for an altitude of 60 km. In conclusion, the overall heat flux and thermal loads on the base region of the vehicle are significantly reduced compared to similar studies by Laureti et al.,⁸ where the effects of secondary bleed nozzles were not considered.

Acknowledgments

The authors would like to thank Mariasole Laureti and Tim Horchler for the helpful discussions and remarks.

References

- [1] P. Brossel, S. Eury, P. Signol, H. Laporte-Weywada, and J.B. Micewics. Development status of the vulcain engine. *31st Joint Propulsion Conference and Exhibit*, 1995.
- [2] Steffen Callsen. Critical analysis of rocket lab neutron launcher and missions. Technical report, März 2022.
- [3] I. B. Celik, U. Ghia, P. J. Roach, C. J. Freitas, H. Coleman, and P. E. Raad. Procedure for estimation and reporting of uncertainty due to discretization in cdf application. *Journal of Fluids Engineering - Transactions of the ASME*, 130(7), July 2008.
- [4] Lance A. Davis. First stage recovery. *Engineering*, 2(2):152–153, 2016.
- [5] Tobias Ecker, Sebastian Karl, Etienne Dumont, Sven Stappert, and Daniel Krause. Numerical study on the thermal loads during a supersonic rocket retropropulsion maneuver. *Journal of Spacecraft and Rockets*, 57(1):131–146, 2020.
- [6] Peter Gerlinger, Helge Möbus, and Dieter Brüggemann. An implicit multigrid method for turbulent combustion. *Journal of Computational Physics*, 167(2):247–276, 2001.
- [7] Klaus Hannemann, Jan M Schramm, Alexander Wagner, Sebastian Karl, and Volker Hannemann. A closely coupled experimental and numerical approach for hypersonic and high enthalpy flow investigations utilising the HEG shock tunnel and the DLR TAU code. Technical report, German Aerospace Center Braunschweig (Germany), Institute of Aerodynamics and Flow Technology, 2010.
- [8] Mariasole Laureti and Sebastian Karl. Aerothermal databases and load predictions for retro propulsion-assisted launch vehicles (retalt). *CEAS Space Journal*, 14(3):501–515, 2022.
- [9] Ansgar Marwege, Josef Klevanski, Johannes Riehmer, Daniel Kirchheck, Sebastian Karl, Davide Bonetti, J. Vos, Matthew Jevons, Anett Krammer, and João Carvalho. Retro propulsion assisted landing technologies (retalt): Current status and outlook of the eu funded project on reusable launch vehicles. In *Paper presented at the 70th International Astronautical Congress, 21-25 October 2019, Washington D.C., United States*, October 2019. Paper presented at the 70th International Astronautical Congress, 21-25 October 2019, Washington D.C., United States www.iafastro.org.
- [10] D. Schwamborn, T. Gerhold, and R. Heinrich. The dlr tau-code: recent applications in research and industry. 2006.
- [11] Martin Sippel, Armin Herbertz, Holger Burkhardt, Takayuki Imoto, Dietrich Haeseler, and Andreas Götz. Studies on expander bleed cycle engines for launchers. In *39th AIAA/ASME/SAE/ASEE Joint Propulsion Conference and Exhibit*, page 4597, 2003.
- [12] Philippe Spalart and Steven Allmaras. A one-equation turbulence model for aerodynamic flows. *AIAA*, 439, 01 1992.
- [13] Ames Research staff. Equations, tables and charts for compressible flow. *NACA report 1135*, 1953.
- [14] Ben Thornber, A. Mosedale, Dimitris Drikakis, David Youngs, and R.J.R. Williams. An improved reconstruction method for compressible flows with low mach number features. *Journal of Computational Physics*, 227:4873–4894, 05 2008.
- [15] Yasuhiro Wada and Meng Liou. A flux splitting scheme with high-resolution and robustness for discontinuities. *32nd Aerospace Sciences Meeting and Exhibit*, 07 1994.